Electromagnetic interference shielding MWCNT-Fe$_3$O$_4$@Ag/epoxy nanocomposites with satisfactory thermal conductivity and high thermal stability

Lei Wang [a,1], Hua Qiu [a,1], Chaobo Liang [a], Ping Song [a], Yixin Han [a], Yixuan Han [a], Junwei Gu [a,b,*], Jie Kong [a], Duo Pan [c,d], Zhanhu Guo [d,**]

[a] MOE Key Laboratory of Material Physics and Chemistry Under Extraordinary Conditions, Shaanxi Key Laboratory of Macromolecular Science and Technology, Department of Applied Chemistry, School of Science, Northwestern Polytechnical University, Xi' an, Shaanxi, 710072, China
[b] Institute of Intelligence Material and Structure, Unmanned System Research Institute, Northwestern Polytechnical University, Xi'an, Shaanxi, 710072, China
[c] College of Chemical and Environmental Engineering, Shandong University of Science and Technology, Qingdao, Shandong, 266590, China
[d] Integrated Composites Laboratory (ICL), Department of Chemical & Biomolecular Engineering, University of Tennessee, Knoxville, TN, 37996, USA

ARTICLE INFO

ABSTRACT

Hierarchical composite nanoparticles of multiwall carbon nanotube (MWCNT)-Fe$_3$O$_4$@Ag combining electrical conductivity and magnetism were obtained from acyl-amine reaction between carboxylation of Fe$_3$O$_4$@Ag (Fe$_3$O$_4$@Ag-COOH) nanoparticles and amino functionalized MWCNTs (MWCNTs-NH$_2$). Finally, the MWCNT-Fe$_3$O$_4$@Ag/epoxy nanocomposites were fabricated via blending-casting method. When the mass ratio of MWCNTs-NH$_2$ to Fe$_3$O$_4$@Ag-COOH was 9:1 (MF-10), the corresponding epoxy nanocomposites presented an optimal electrical conductivity and electromagnetic interference (EMI) shielding effectiveness (SE). Furthermore, the MF-10/epoxy nanocomposites with 15 wt% MF-10 presented a satisfying EMI SE of 35 dB and high electrical conductivity of 0.280 S/cm, satisfactory thermal conductivity (thermally conductive coefficient, λ of 0.46 W/mK), outstanding Young's modulus of 4.60 GPa & hardness value of 0.26 GPa and excellent thermal stability (T_{HRI} of 183.4 °C). The introduction of Fe$_3$O$_4$@Ag nanoparticles not only enhanced the interaction among MF-10, so as to promote the formation of conductive networks, leading to higher λ and EMI SE value, but also contributed to hysteresis loss of electromagnetic waves, and offered more interfaces to reflect and reabsorb electromagnetic waves, resulting in highly improved attenuation of electromagnetic waves.

© 2018 Elsevier Ltd. All rights reserved.

1. Introduction

With the rapid development of modern aviation electronic technology, the transmission power of the mission system is getting larger, and the corresponding influences on other systems and workers become more and more serious [1,2]. Under this background, it would be significant for the development of aviation weapons & equipments to design & investigate aircraft structures with electromagnetic interference (EMI) shielding performance.

Compared to conventional metal-based EMI shielding materials, polymeric composites present potential applications in EMI shielding fields, owing to their lightweight, excellent corrosion resistance and easy processing & fabrication, etc. [3–5]. Generally, polymer-based EMI shielding materials are divided into two types: intrinsic type and compound type. However, the poor mechanical and processing properties of intrinsic type electrically conductive polymers have restricted their applications in EMI shielding [6]. While the compound type EMI shielding polymeric composites present the advantage of one-time molding process. And

incorporating fillers into polymeric matrix is considered to be one of the most effective ways to fabricate the EMI shielding materials (compound type), due to their easy processing and adjustable EMI shielding performance by changing the filler content [7]. Silver, copper, nickel and carbon materials [8] are generally used as the conductive fillers. Herein, carbon nanotubes (CNTs) with excellent elastic modulus, electrical and thermal conductivity, have presented promising applications in EMI shielding fields. For example, Huang et al. [9] prepared single-walled CNTs (SWCNTs)/epoxy composites, and the EMI shielding effectiveness (SE) of the obtained 5 wt% SWCNTs/epoxy composite reached 15–20 dB (500 MHz–1.5 GHz). Furthermore, Li et al. [4] reported the maximum EMI SE of the SWCNTs/epoxy composites reached 24 dB at X-band (8–12 GHz) by introducing SWCNTs into epoxy matrix. Liu et al. [10] improved the dispersion of CNTs in epoxy matrix by fluorinated modification, and the obtained EMI SE of the CNTs/epoxy nanocomposites reached 28 dB (1 GHz–8 GHz).

However, it remains challenging to achieve the targeted EMI SE only by addition of CNTs [9]. So far, hybrid fillers of CNTs and magnetic nanoparticles (such as Fe [11], Ni [12], Co ferrites [13] and their multi-component ferrites like Fe_3O_4 [14], MnO_2 [15], CrO_2, *etc.*) were synchronously introduced to fabricate the EMI shielding nanocomposites. Herein, the Fe_3O_4 nanoparticles are frequently-used magnetic nanoparticles [16]. Combining CNTs with Fe_3O_4 nanoparticles will further broaden their applications [17] for strengthening the magnetic hysteresis loss of the obtained composites. Fu et al. [18] coated CNTs with Fe_3O_4 nanoparticles *via* solvothermal method. The loss for electromagnetic waves was significantly improved, which was strongly depended on the magnetic coating structure. Chaudhary et al. [19] fabricated the conductive paper by synchronously introducing carbon microspheres, Fe_3O_4 and CNTs. The obtained EMI SE of the conductive paper was increased by nearly 50% with the introduction of Fe_3O_4 nanoparticles. However, the introduction of Fe_3O_4 nanoparticles often leads to a decrease in electrical conductivity. According to the previous researches [20,21], coating the Fe_3O_4 nanoparticles with silver could be in favor of improving the electrical conductivity. Sun et al. [22] reported the increased conductivity from 2.5×10^{-3} to 64.7 S/cm by overlaying of Fe_3O_4 with silver. However, to our knowledge, adopting hybrid fillers of CNTs and Fe_3O_4@Ag nanoparticles to fabricate the electromagnetic shielding polymeric nanocomposites has hardly been reported till now.

As one of high performance thermosetting resins, epoxy resins possess excellent comprehensive properties (high mechanical properties [23] & adhesion strength [24], good electrical insulation [25], excellent dimensional & thermal stabilities [26], high solvent resistance [27], and ease of processing [25], *etc.*), and have been widely applied as the matrix of coatings, adhesives and composites.

Herein, we proposed a novel approach to prepare epoxy EMI shielding nanocomposites. The Fe_3O_4@Ag-COOH core-shell nanoparticles were firstly synthesized by functionalizing the Fe_3O_4 nanoparticles with silver and 11-mercaptoundecanoic acid (MUA) [28,29]. Meanwhile, MWCNTs-NH_2 were also obtained by amino functionalization of MWCNTs. And the hierarchical composite nanoparticles of MWCNT-Fe_3O_4@Ag combining with electrical conductivity and magnetism were then obtained from the acyl-amine reaction between Fe_3O_4@Ag-COOH nanoparticles and MWCNTs-NH_2 (as shown in Scheme 1). Finally, the MWCNT-Fe_3O_4@Ag/epoxy EMI shielding nanocomposites were then fabricated *via* blending-casting method. The corresponding structures and morphologies of the Fe_3O_4@Ag-COOH, MWCNTs-NH_2 and MWCNT-Fe_3O_4@Ag were explored and characterized by transmission electron microscope (TEM), thermal gravimetric analyses (TGA), Fourier transform infrared spectra (FTIR), X-ray photoelectron spectroscopy (XPS) and Raman spectrum, *etc*. The optimum
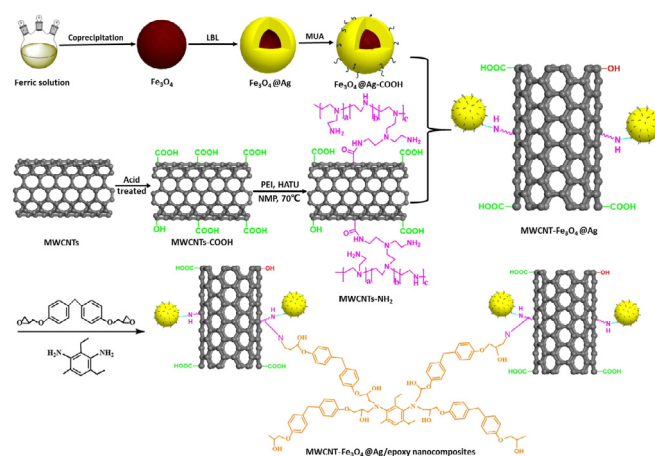
Scheme 1. Schematic diagram of general fabrication process of MWCNT-Fe_3O_4@Ag/epoxy nanocomposites; LBL was the abbriviation of "layer-by-layer method".

ratio of Fe_3O_4@Ag-COOH to MWCNTs-NH_2 was determined according to EMI SE value of the obtained epoxy nanocomposites. Furthermore, the effects of the MWCNT-Fe_3O_4@Ag contents on the EMI SE, electrical conductivity, thermal conductivity, mechanical and thermal properties of the obtained MWCNT-Fe_3O_4@Ag/epoxy nanocomposites were discussed and investigated.

2. Experiment section

2.1. Materials

MWCNTs (~50 μm in length, 98% purity) were obtained from Chengdu Organic Chem. Co. (Chengdu, China). $FeCl_2 \cdot 4H_2O$, tetramethylammonium hydroxide pentahydrate (TMAOH), sodium citrate, diisopropylethylamine (DIEA), $NaBH_4$ and $NH_2OH \cdot HCl$ were all purchased from Alfa Aesar (Shanghai, China). Sodium citrate, N-methyl-pyrrolidone (NMP), $FeCl_3 \cdot 6H_2O$ and $AgNO_3$ were all received from J&K Chemicals (Shanghai, China). Polyethyleneimine (PEI, w.t. 600), 11-mercaptoundecanoic acid (MUA), diisopropylethylamine (DIEA) and N-[(dimethylamino)methylene]-1H-1,2,3-triazolo-[4, 5-b]-pyridin-1-ylmethylene]-N-methylmethanaminium hexafluorophosphate N-oxide (HATU) were all purchased from Macklin (Shanghai, China). Bisphenol F epoxy (Epon 862) and curing agent of 2, 4-diethyl-6-methylbenzene-1,3-diamine (EK 3402) were both provided by Hexion Inc (Columbus, USA).

2.2. Preparation of MWCNT-Fe_3O_4@Ag 2.2.1 preparation of Fe_3O_4@Ag-COOH nanoparticles

The synthesis of Fe_3O_4@Ag-COOH core-shell nanoparticles was similar to our previous work [30], despite the oxidation of Fe_3O_4 to Fe_2O_3 and $AgNO_3$ instead of $HAuCl_4$, the dosage of the other chemicals was the same.

2.2.1. Preparation of MWCNTs-NH_2

Carboxylation of MWCNTs (MWCNTs-COOH) was prepared by refluxing 1 g pristine MWCNTs in a mixed acid of H_2SO_4/HNO_3 (1:3 by volume) at 90 °C for 90 min. The obtained products were collected by vacuum filtering and washed with deionized water until the pH value reached 7, and dried in vacuum at 60 °C for 12 h. Then 100 mg MWCNTs-COOH, 200 mg HATU and 200 mg DIEA were added into 30 mL N-Methyl-2-pyrrolidone (NMP) solution, and sonicated for 2 h. Subsequently, 10 mL NMP solution containing 300 mg PEI was added. The above mixtures were maintained and reacted at 130 °C under refluxing for 4 h, followed by vacuum

filtered and washed with methanol. Finally, the obtained products were dried in vacuum at 60 °C for 12 h. 2.2.3 Preparation of MWCNT-Fe$_3$O$_4$@Ag.

30 mg Fe$_3$O$_4$@Ag-COOH, 200 mg HATU and 200 mg DIEA were added into 30 mL NMP solution, and then sonicated for 2 h. Consequently, the obtained mixtures were then added dropwise into NMP solution containing different loadings of MWCNTs-NH$_2$. The above mixtures were kept reaction at 130 °C for 4 h, followed by centrifugation with methanol for three times and dried in vacuum at 60 °C for 12 h. The obtained product was named as MF for neat MWCNT-Fe$_3$O$_4$@Ag, whereas MF-5, MF-10, MF-15 and MF-20 named for 5, 10, 15, and 20 wt% of Fe$_3$O$_4$@Ag-COOH loading in MWCNT-Fe$_3$O$_4$@Ag, respectively.

2.3. Preparation of MWCNT-Fe$_3$O$_4$@Ag/epoxy electromagnetic shielding nanocomposites

Epon 862 and appropriate MWCNT-Fe$_3$O$_4$@Ag were mechanically stirred for 2 h at room temperature, followed by adding EK 3402. The above mixtures were stirred uniformly at 70 °C, degassed in a vacuum vessel to remove air bubbles, and then poured into the preheated mold. Finally, the obtained mixtures above were cured at 120 °C for 5 h and cooled down to room termperature naturally, finally the MWCNT-Fe$_3$O$_4$@Ag/epoxy electromagnetic shielding nanocomposites were obtained.

2.4. Characterizations

TEM images were collected on a Talos F200X/TEM microscope (FEI Company) operated at 200 kV. XPS analyses of the samples were performed on a PHI5400 equipment (PE Corp., England). The magnetic properties of the samples were investigated using a vibrating sample magnetometer (VSM) at room temperature. All the UV−Vis spectra were performed on a Shimadzu UV-2550 spectrophotometer. Raman spectrum was collected on a Renishaw micro-Raman with a Ti-Safire laser, tuned at 785 nm. TGA of the samples were carried out using STA 449F3 (Netzsch C Corp., Germany) at 10 °C/min^{-1} (air condition), over the entire temperature range (40−900 °C). X-ray diffraction (XRD) crystallography was obtained on a PhillipsPW3040-MPD diffractometer (copper K-radiation = 1.5418 Å). FTIR spectra of the samples were captured on Bruker Tensor 27 equipment (Bruker Co., Germany) with thin films on KBr. The nanoindentation technique was employed to evaluate the samples' mechanical properties (modulus, hardness, and creep behavior). The indentation experiment was performed with a G200 nanoindenter from Agilent. The peak indentation load was set as 9 mN with the fixed loading and unloading rates of 300 and 450 mN/s, respectively. The dwell time at the maximum load was 5 s. To avoid the interference among the different indents, the intervals among any neighboring indents were greater than 100 mm. To get statistically significant results, at least 36 indents were conducted on each sample. The electrical conductivity of the samples was measured by a four-probe method at room temperature. S-parameters of the samples, which corresponded to the reflection (S11 and S22) and transmission (S12 and S21) of transverse electromagnetic waves, were measured by a VNA (MS4644A, Anritsu) using the wave-guide method in the X-band frequency range (8.2−12.4 GHz) according to ASTM D5568-08, and the corresponding specimen dimension was 22.86 mm × 10.16 mm × 2 mm.

3. Results and discussion

3.1. Fe$_3$O$_4$@Ag-COOH nanoparticles

FTIR spectra of Fe$_3$O$_4$ and Fe$_3$O$_4$@Ag-COOH nanoparticles are

depicted in Fig. 1(a). It was clear that the peaks at 3413 cm^{-1} and 1626 cm^{-1} were ascribed to the characteristic absorption of -OH group. During the chemical co-precipitation, some hydroxyl groups covered the surfaces of magnetite in an aqueous environment [31]. The peak at 583 cm^{-1} was assigned to the characteristic absorption of Fe-O group [32]. For Ag coated by MUA, the bands appeared at 2916 cm^{-1} and 2846 cm^{-1} were assigned to the characteristic absorption peaks of ν (CH$_2$) and ν_s (CH$_2$) modes of MUA [33], and the peak at 1642 cm^{-1} was ascribed to the characteristic absorption of C=O group, which confirmed the successful introduction of MUA onto the surface of Fe$_3$O$_4$@Ag nanoparticles. Fig. 1(b) presented the wide-scan XPS spectrum of Fe$_3$O$_4$ nanoparticles. The peaks at 54.0 eV, 711.0 eV and 724.0 eV were corresponded to the characteristic doublets of Fe 3P, Fe 2P$_{3/2}$ and Fe 2P$_{1/2}$, consistent with the reported values for Fe$_3$O$_4$ [34]. For Fe$_3$O$_4$@Ag-COOH nanoparticles, all the characteristic peaks of Fe disappeared, and the new peaks at 368.0, 374.0 and 229.0 eV were ascribed to Ag 3d$_{5/2}$, Ag 3d$_{3/2}$ and S 2s [35], indicating that the MUA had been deposited on the surface of Fe$_3$O$_4$@Ag nanoparticles. As shown in Fig. 1(c) and (c'), the spherical Fe$_3$O$_4$ nanoparticles synthesized *via* co-precipitation method presented a uniform average size about 10.3 ± 1.8 nm, and aggregated due to magnetic force. After coated with Ag, the size was increased to 13.1 ± 2.4 nm. Results of Kolmogorov-Smirnov tests revealed that the corresponding nanoparticle sizes conformed to a normal distribution. And the HRTEM image of Fe$_3$O$_4$@Ag-COOH NPs is also shown in Fig. 1(c''). It confirmed the Fe$_3$O$_4$@Ag-COOH NPs possessed the core-shell structure, and the corresponding particle size of the Fe$_3$O$_4$ core was about 10.7 nm and the thickness of silver shell was about 2.7 nm.

Furthermore, the dispersion of Fe$_3$O$_4$@Ag-COOH nanoparticles in water was also improved obviously. The UV−vis absorption spectra of Fe$_3$O$_4$ and Fe$_3$O$_4$@Ag-COOH nanoparticles are shown in Fig. 1(d). The as-prepared Fe$_3$O$_4$@Ag nanoparticles presented obvious plasmon peak in the range of 350−450 nm [36], while Fe$_3$O$_4$ nanoparticles exhibited no absorption peak over the entire range from 300 to 800 nm, which was attributed that Fe$_3$O$_4$ nanoparticles were coated with Ag shell. Fig. 1(e) shows the XRD patterns for Fe$_3$O$_4$ and Fe$_3$O$_4$@Ag-COOH nanoparticles. Six characteristic peaks (2θ = 30.1, 35.5, 43.1, 53.4, 57.0, and 62.6°) were observed in the XRD pattern of Fe$_3$O$_4$ nanoparticles, marking their indices ((220), (311), (400), (422), (511), and (440)), in accordance with those reported in previous literature [37]. And in the XRD pattern of Fe$_3$O$_4$@Ag-COOH nanoparticles, the four new appeared peaks were attributed to the indices ((111), (200), (220), and (311)) of silver [38]. Furthermore, the magnetic properties of Fe$_3$O$_4$ and Fe$_3$O$_4$@Ag-COOH were studied by vibrating sample magnetometer
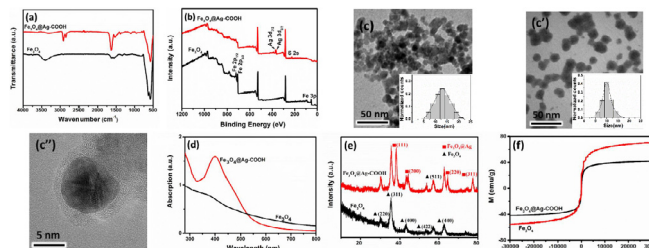

Fig. 1. (a) FTIR spectra of Fe$_3$O$_4$ and Fe$_3$O$_4$@Ag-COOH nanoparticles; (b) wide-scan XPS spectra of Fe$_3$O$_4$ and Fe$_3$O$_4$@Ag-COOH nanoparticles; TEM images of (c) Fe$_3$O$_4$ and (c') Fe$_3$O$_4$@Ag-COOH nanoparticles. Insets: histograms of the particle diameters for (c) 118 particles, (c') 81 particles; (c'') HRTEM image of Fe$_3$O$_4$@Ag-COOH nanoparticle. (d) UV−vis absorption spectra of Fe$_3$O$_4$ and Fe$_3$O$_4$@Ag-COOH nanoparticles; (e) XRD patterns for Fe$_3$O$_4$ and Fe$_3$O$_4$@Ag-COOH nanoparticles; (f) Magnetization curves of Fe$_3$O$_4$ and Fe$_3$O$_4$@Ag-COOH nanoparticles. (A colour version of this figure can be viewed online.)

(VSM) at room temperature (seen in Fig. 1(f)). There was no significant coercivity in their hysteresis loops, indicating a superparamagnetic feature. The saturation magnetization of $Fe_3O_4@Ag$-COOH nanoparticles was determined to be 42.1 emu·g^{-1}, lower than that of Fe_3O_4 nanoparticles (70.0 emu·g^{-1}) due to the non-magnetic silver and others.

3.2. MWCNTs-NH₂

Fig. 2 (a) presents the Raman spectra of the MWCNTs. It could be observed that the peak at 130 cm^{-1} and 180 cm^{-1} was ascribed to the semiconductor-like and metallic carbon nanotubes [39], respectively. It indicated that the purchased MWCNTs were composed of semiconductor-like and metallic carbon nanotubes. Fig. 2 (b&b') shows the TEM images of MWCNTs and MWCNTs-NH₂. It could be seen that the MWCNTs with heavy agglomeration presented a relatively larger length/diameter ratio. After the surface treatment by mixed acid and functionalization with PEI, the length/diameter ratio of MWCNTs-NH₂ was decreased and the dispersibility in ethanol for MWCNTs-NH₂ was improved obviously, mainly ascribed to rich −COOH [40] and -NH₂ groups on the surface of the MWCNTs-NH₂ [41]. Fig. 2(c) shows the FTIR spectra of MWCNTs and MWCNTs-NH₂. There was no absorption peak for MWCNTs, while MWCNTs-NH₂ presented four new absorption peaks at 3410, 1703, 1560 and 1203 cm^{-1}, corresponded to the stretching vibration of amide group [42], -C=O [43], primary amine [44] and C-N groups, respectively. It confirmed that the PEI had been grafted onto MWCNTs successfully. Fig. 2(d) shows the wide-scan XPS spectra of MWCNTs and MWCNT-NH₂, and the corresponding XPS results are shown in Table 1. Compared to that of MWCNTs, the appearance of N 1s peak at 400.0 eV [45] of MWCNT-NH₂ was assigned to the nitrogen element of PEI. Fig. 2(d') and Fig. 2(d'') show the high resolution of the C1s XPS spectra of MWCNTs and MWCNTs-NH₂, respectively. And detailed information about peak fitting is summarized in Table 2. Compared to that of Fig. 2(d'), the proportion of C=C (284.4 eV) and C-C (285.4 eV) of MWCNTs-NH₂ was decreased, and there were three new peaks at 286.8 eV, 287.8 eV and 289.21 eV, ascribed to C-O/C-N, C=C and COO/CON, respectively. Results further confirmed that PEI had been successfully grafted onto MWCNTs.

3.3. MWCNT-Fe₃O₄@Ag

Fig. 3 (a) shows the TEM images of MF-5, MF-10, MF-15 and MF-20. The content of the $Fe_3O_4@Ag$-COOH nanoparticles on the surface of MWCNTs-NH₂ was normally increased with increasing the

Table 1
XPS results for MWCNTs and MWCNTs-NH₂.

Samples	C (%)	O (%)	N (%)
MWCNTs	96.90	3.10	–
MWCNTs-NH₂	73.07	20.31	6.62

Table 2
XPS C1s curve fitting results for MWCNTs and MWCNTs-NH₂.

Types	C=C (%)	C-C (%)	C-O/C-N (%)	C=O (%)	O=C-O/O=C-N (%)
MWCNTs	30	70	–	–	–
MWCNTs-NH₂	17.38	63.74	9.51	2.86	6.51

addition of $Fe_3O_4@Ag$-COOH nanoparticles. There were few $Fe_3O_4@Ag$-COOH nanoparticles on the surface of MWCNTs-NH₂ for MF-5, while some aggregations were formed for MF-15 and MF-20. Compared with that of MWCNTs-NH₂ (Fig. 3(b)), all the MF-5, MF-10, MF-15 and MF-20 showed the absorption peaks of V (CH₂) and Vs (CH₂) patterns, revealing the successful introduction of $Fe_3O_4@Ag$-COOH nanoparticles on the surface of MWCNTs-NH₂. Moreover, all the peaks corresponded to amide, -C=O, primary amine and -NH groups, are mainly ascribed to the reaction between $Fe_3O_4@Ag$-COOH nanoparticles and MWCNTs-NH₂. Fig. 3(c) and (d) present the XPS spectra and TGA curves of MF-5, MF-10, MF-15 and MF-20, and the obtained results are summarized in Table 3. Fig. 3 (c') shows the wide-scan XPS spectra of MF-5, MF-10, MF-15 and MF-20 from 450.0 eV to 350.0 eV. The increase of Ag element and decrease of N element also proved the acyl-amine reaction between $Fe_3O_4@Ag$-COOH nanoparticles and MWCNTs-NH₂. The high resolution of the C1s XPS spectra of MF-5, MF-10, MF-15, and MF-20 is also shown in Fig. 3(c''), Fig. 3 (c'''), Fig. 3(c'''') and Fig. 3(c'''''), respectively. The corresponding information about peak fitting is shown in Table 4. Compared to that of MWCNTs-NH₂, the proportion of C=C (284.4 eV) ascribed from MWCNTs and C-O/C-N (286.5 eV) decreased, and C-C (285.4 eV) increased with the addition of $Fe_3O_4@Ag$-COOH nanoparticles. The $Fe_3O_4@Ag$ NPs could not be thermally degraded, while the MWCNTs-NH₂ would be oxidized and volatilized in high temperatures. The residue of the MF-5, MF-10, MF-15 and MF-20 reached about 4.1 wt%, 9.0 wt%, 13.4 wt% and 17.9 wt%, respectively. It indicated that more $Fe_3O_4@Ag$-COOH NPs reacted with MWCNTs-NH₂ with the
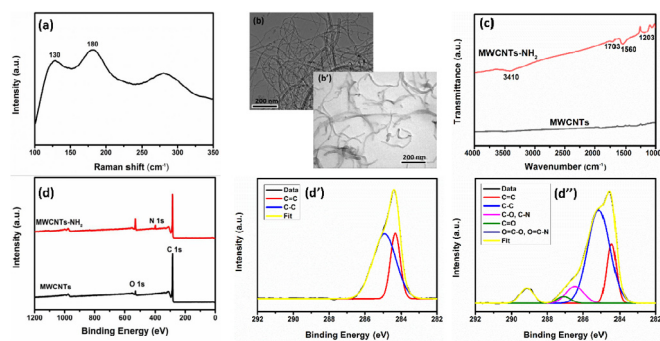

Fig. 2. (a) Raman spectra of MWCNTs. TEM images of (b) MWCNTs and (b') MWCNTs-NH₂; (c) FTIR spectra of MWCNTs and MWCNTs-NH₂; (d) Wide-scan XPS spectra of MWCNTs and MWCNTs-NH₂; High resolution of the C1s XPS spectra of (d') MWCNTs and (d'') MWCNTs-NH₂, respectively. (A colour version of this figure can be viewed online.)
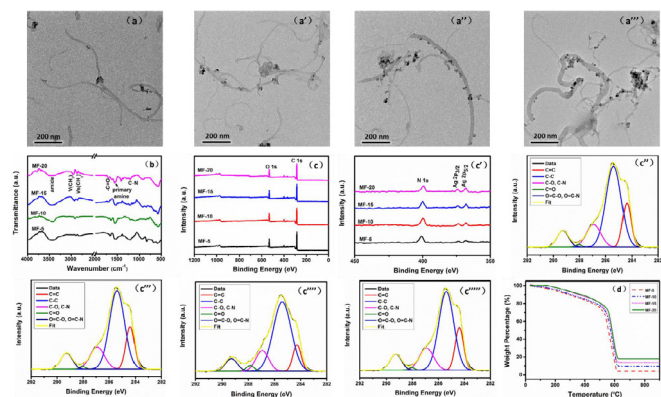

Fig. 3. TEM images of (a) MF-5, (a') MF-10, (a'') MF-15 and (a''') MF-20; (b) FTIR spectra for MF-5, MF-10, MF-15 and MF-20; (c) Wide-scan XPS spectra of MF-5, MF-10, MF-15 and MF-20; (c') Wide-scan XPS spectra of MF-5, MF-10, MF-15 and MF-20 from 450.0 eV to 350.0 eV. The high resolution of the C1s XPS spectra of (c'') MF-5, (c''') MF-10, (c'''') MF-15 and (c''''') MF-20, respectively; (d) TGA curves of MF-5, MF-10, MF-15 and MF-20. (A colour version of this figure can be viewed online.)

Table 3
XPS and TGA results for MF-5, MF-10, MF-15 and MF-20.

Samples	C (%)	O (%)	N (%)	Ag (%)	Residue (wt%)
MF-5	61.6	31.4	6.2	0.8	4.1
MF-10	61.2	31.8	5.3	1.7	9.0
MF-15	61.6	30.8	4.8	2.8	13.4
MF-20	60.4	31.5	4.5	3.6	17.9

Table 4
XPS C1s curve fitting results for MF-5, MF-10, MF-15 and MF-20.

Types	C=C (%)	C-C (%)	C-O/C-N (%)	C=O (%)	O=C-O/O=C-N (%)
MF-5	16.36	58.55	15.45	0.75	8.89
MF-10	15.04	60.65	14.72	0.77	8.83
MF-15	13.23	62.92	13.81	1.38	8.66
MF-20	11.66	66.74	11.51	1.80	8.29

increasing addition of Fe_3O_4@Ag-COOH NPs. The above analyses and results further proved that more Fe_3O_4@Ag-COOH nanoparticles were decorated on the surface of MWCNTs-NH_2.

3.4. MWCNT-Fe₃O₄@Ag/epoxy nanocomposites

Fig. 4 **(a)** depicts the electrical conductivity of epoxy nanocomposites filled with MWCNTs, MWCNTs-NH_2, MF-5, MF-10, MF-15 and MF-20. The electrical conductivity of epoxy nanocomposites filled with 5 wt% MWCNTs-NH_2 was decreased from 0.0186 S/cm (5 wt% MWCNTs) to 0.0158 S/cm, mainly ascribed to the structural damage and produced disordered sites of MWCNTs after carboxylation treatment by strong acids [46]. For a given filler loading (5 wt% and 10 wt%), the electrical conductivity of the MWCNT-Fe_3O_4@Ag/epoxy nanocomposites was all higher than that of MWCNT/epoxy nanocomposite, except MF-20/epoxy nanocomposite. Herein, MF-10/epoxy nanocomposites with 10 wt% MF-10 presented the maximum electrical conductivity value of 0.226 S/cm. On one hand, the improved interfacial compatibility between MWCNT-Fe_3O_4@Ag and epoxy matrix could be in favor of increasing the dispersion of MWCNT-Fe_3O_4@Ag inner epoxy matrix [47], also beneficial to the rapid formation of conductive networks. On the other hand, compared with that of single MWCNTs, the addition of Fe_3O_4@Ag on the side-wall of the MWCNTs was more likely for the contacting possibility between MWCNT-Fe_3O_4@Ag, which was conducive to the formation of conductive networks. Meantime, the magnetic properties of the MWCNT-Fe_3O_4@Ag were also enhanced with the introduction of Fe_3O_4@Ag-COOH, which could help the contact of MWCNT-Fe_3O_4@Ag. Electrons could not only transfer by contact between MF, but also form electric current by electron transition. As a result, the electrical conductivity was improved after the introduction of Fe_3O_4@Ag-COOH nanoparticles.

In our work, MWCNTs played the main role in the conductive networks. In fact, the mass fraction of the MWCNTs was decreased with the increasing content of Fe_3O_4@Ag NPs, and the

corresponding ability to transfer electrons was also weakened. Therefore, the electrical conductivity of MF-15/epoxy nanocomposite and MF-20/epoxy nanocomposite were both dropped down. Fortunately, the epoxy nanocomposites with 10 wt% MF-20 still maintained the same electrical conductivity value with that of epoxy nanocomposites with 10 wt% MWCNTs.

Fig. 4(b and c) illustrates the EMI SE for epoxy nanocomposites at X-band filled with MWCNTs, MWCNTs-NH_2, MF-5, MF-10, MF-15 and MF-20 (5 wt% for (b) and 10 wt% for (c), respectively). For a given filler loading (5 and 10 wt%), all the MWCNT-Fe_3O_4@Ag/epoxy nanocomposites presented relatively higher average EMI SE values in comparison to those of the MWCNTs/epoxy and MWCNTs-NH_2/epoxy nanocomposites. The epoxy nanocomposites with 10 wt% MF-10 presented the maximum EMI SE value of 26 dB, increased by 51% compared to that of MWCNTs/epoxy nanocomposite (17 dB for 10 wt% MWCNTs). When incident waves stroked the shield, a portion of the waves was reflected back and absorbed via interacting with surface charges. The transmitted waves would be further multiply reflected and reabsorbed. One hand, MWCNT-Fe_3O_4@Ag/epoxy nanocomposites possessed higher conductivity than those of MWCNTs/epoxy nanocomposites, which would discourage the impedance matching. Therefore, it could cause more electromagnetic waves to be reflected back and reabsorbed, resulting in the improvement of the EMI SE. On the other hand, the addition of Fe_3O_4@Ag nanoparticles could contribute to the hysteresis and dielectric loss for electromagnetic waves, thus improving the attenuation of the electromagnetic waves [48]. As a result, the MWCNT-Fe_3O_4@Ag/epoxy nanocomposites showed relatively higher average EMI SE values in comparison to those of the MWCNTs/epoxy and MWCNTs-NH_2/epoxy nanocomposites.

Furthermore, for the MF-10/epoxy nanocomposites with the optimal electrical conductivity, MWCNTs also played the leading role in absorbing electromagnetic waves. With the increasing addition of Fe_3O_4@Ag nanoparticles, the relative content of MWCNTs was decreased. Excessive addition of Fe_3O_4@Ag nanoparticles not only decreased the conductivity of the MF-10/epoxy nanocomposites, but also decreased the ability of absorb electromagnetic waves for MWCNTs. Therefore, there would be a balance point of content between the Fe_3O_4@Ag nanoparticles and MWCNTs. Results revealed that MF-10 was this equilibrium point. It not only enhanced the conductive networks of the MF-10/epoxy nanocomposites, but also presented the strongest attenuation to electromagnetic waves by hysteresis and dielectric loss. Therefore, the optimal EMI SE value was obtained for the MF-10/epoxy nanocomposite, which was slightly higher than that of MF-15/epoxy nanocomposite and MF-20/epoxy nanocomposite. In addition, the obtained EMI SE MWCNTs/epoxy nanocomposite at f > 12 GHz was slightly higher than the MF-20/epoxy nanocomposite due to the fluctuation of EMI SE curves.

3.5. MF-10/epoxy nanocomposites

To our knowledge, the percolation theory [9] was more applicable to guide and verify our system. Fig. 5(a) shows the electrical conductivity of MF-10/epoxy nanocomposites as a function of MF-10 content. The electrical conductivity of the epoxy nanocomposites was increased with increasing the addition of MF-10. The MF-10/epoxy nanocomposites with 15 wt% MF-10 possessed the maximum electrical conductivity of 0.280 S/cm, and the corresponding conductivity percolation phenomenon was occurred near 1 wt% MF-10.

The total EMI SE (SE_T, Fig. 5(b)), absorption SE (SE_A, Fig. 5(c)) and reflection SE (SE_R, Fig. 5(d)) values of the MF-10/epoxy nanocomposites were also compared and analyzed. With increasing the addition of MF-10, both SE_T and SE_A values were increased
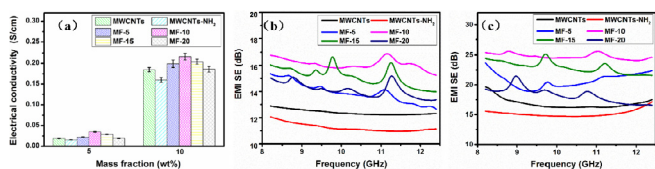

Fig. 4. (a) Electrical conductivity of epoxy nanocomposites with 5 wt% and 10 wt% MWCNTs, MWCNTs-NH_2, MF-5, MF-10, MF-15 and MF-20; EMI SE for epoxy nanocomposites with (b) 5 wt% and (c) 10 wt% MWCNTs, MWCNTs-NH_2, MF-5, MF-10, MF-15 and MF-20 at X-band. (A colour version of this figure can be viewed online.)
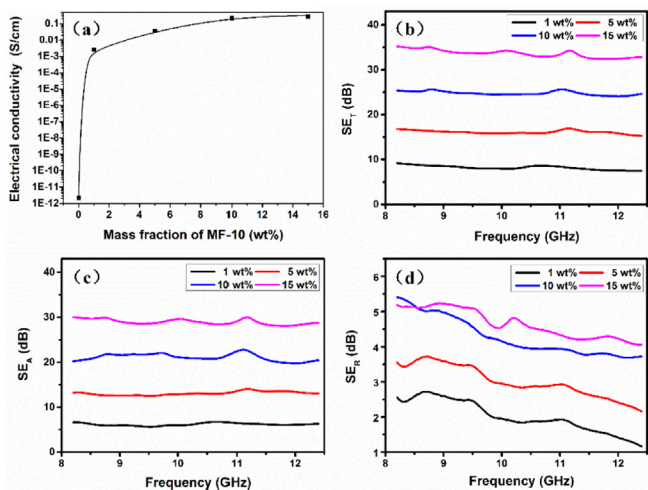
Fig. 5. (a) Log electrical conductivity *vs* mass fraction of MF-10; EMI SE for MF-10/epoxy nanocomposites at X-band: (b) SE_T, (c) SE_A, (d) SE_R. (A colour version of this figure can be viewed online.)

Fig. 6. Mass fraction of MF-10 affecting the λ and a values of the MF-10/epoxy nanocomposites. (A colour version of this figure can be viewed online.)

Table 5
EMI shielding performance of various polymeric composites.

Filler	Matrix	Content	Thickness (mm)	Conductivity (S/cm)	EMI SE (dB)	Frequency (GHz)	Ref
Ag Nanowires	PS	2.5 vol%	0.8	0.19	33	8.2–12.4	[53]
Graphite	PE	18.7 vol%	3	/	33	8.2–12.4	[54]
RGO	Epoxy	15 wt%	2	0.10	21	8.2–12.4	[55]
RGO/Fe$_3$O$_4$	PEI	10 wt%	2.5	10^{-6}	18	8.2–12.4	[56]
SWCNTs	Epoxy	15 wt%	2	0.20	25	8.2–12.4	[57]
MWCNTs/Fe$_3$O$_4$/Fe	Epoxy	10 wt%	2	/	26	8.2–12.4	[58]
MF-10	**Epoxy**	**15** wt%	**2**	**0.28**	**35**	**8.2–12.4**	**This work**

"/"- values not provided.

obviously, while the SE_R values were increased slowly. The corresponding SE_T value of the MF-10/epoxy nanocomposites with 15 wt% MF-10 was enhanced to 35 dB, far above that of MWCNTs/epoxy nanocomposites (15 wt% MWCNTs), also higher than that of target value needed for commercial applications (20 dB). It was also observed that the SE_A values were much higher than that of SE_R values, which indicated that SE_A played a leading role in the loss of electromagnetic waves [49]. The differences between SE_A and SE_R values with increasing the addition of MF-10 were ascribed to the interfacial polarization of MF-10/epoxy system [50]. The primary mechanism of EMI shielding was usually a reflection of the electromagnetic radiation incident, due to the interaction of EMI radiation with free electrons on the surface of the shield [51]. The absorption was usually the secondary mechanism of EMI shielding. The electric dipoles in the shield interacted with the electromagnetic fields in the radiation [52]. With increasing the addition of MF-10, the conductive networks were gradually developed, resulted in the increased electrical conductivity and improved EMI SE values. Moreover, the increased frequency of reflection, absorption and hysteresis loss between Fe$_3$O$_4$@Ag and CNTs could improve the attenuation of electromagnetic waves in the MF-10/epoxy nanocomposites.

A comparison with previously reported polymeric composites with similar composition by the blend-compounded method is presented in Table 5. Compared with other works, the obtained MF-10/epoxy nanocomposites with 15 wt% MF-10 in our work presented relatively higher electrical conductivity (0.280 S/cm) and SE value (35 dB) with the same thickness and/or lower thickness. It indicated that MF-10 was a good candidate for the promising EMI shielding. The reason was that the introduction of Fe$_3$O$_4$@Ag-COOH
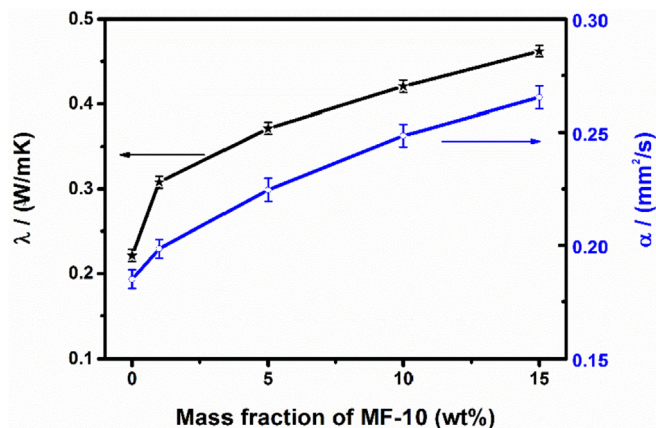
nanoparticles not only contributed to hysteresis and dielectric loss to electromagnetic waves, but also strengthened the connection between MWCNTs, promoting the formation of conductive networks. As a result, the corresponding EMI SE value in the X-band was improved.

Fig. 6 presents the mass fraction dependence of MF-10 on the thermally conductive coefficient (λ) and thermal diffusivity (a) values of the MF-10/epoxy nanocomposites. Higher λ and a values of the MF-10/epoxy nanocomposites could be achieved with higher MF-10 content. And the λ and a values of the epoxy nanocomposites with 15 wt% MF-10 were increased to 0.46 W/mK and 0.27 mm^2/s, increased by 129.6% and 43.0% for that of pure epoxy matrix (λ of 0.22 W/mK and a of 0.19 mm^2/s), respectively. The reason was mainly attributed to the enhanced touching & connecting probability of the MF-10 [59], in favor of forming more effectively thermally conductive channels [60], finally to increase the λ and a values of the MF-10/epoxy nanocomposites.
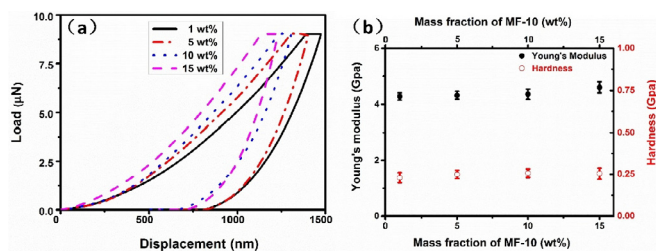

Fig. 7. Mass fraction of MF-10 on the hardness and Young's modulus of the MF-10/epoxy nanocomposites. (a) The representative load-displacements; (b) Hardness and Young's modulus. (A colour version of this figure can be viewed online.)
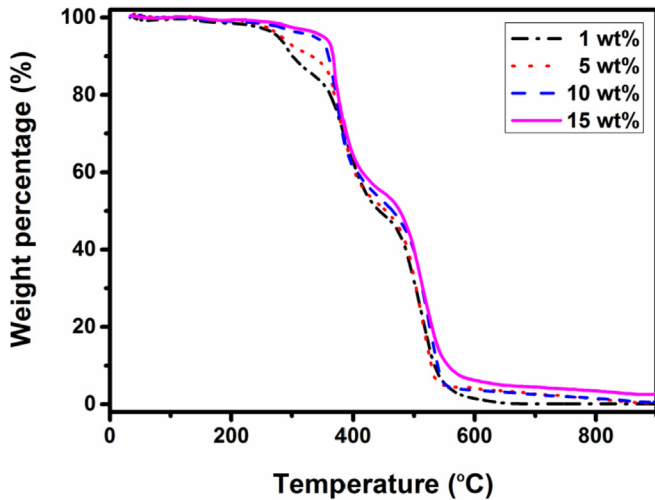
Fig. 8. TGA curves of the MF-10/epoxy nanocomposites. (A colour version of this figure can be viewed online.)

T_5 and T_{30} is corresponding decomposition temperature of 5% and 30% weight loss, respectively.

4. Conclusions

The novel hierarchical composite nanoparticles of MWCNTs-Fe_3O_4@Ag combining electrical conductivity and magnetism were firstly obtained from the acyl-amine reaction between Fe_3O_4@Ag-COOH nanoparticles and MWCNTs-NH_2. TEM, TGA, FTIR, XPS and Raman analyses revealed that the nanoparticles of Fe_3O_4@Ag-COOH, MWCNTs-NH_2 and their compound of MWCNT-Fe_3O_4@Ag were obtained successfully. When the mass ratio of MWCNTs-NH_2 to Fe_3O_4@Ag-COOH was 9:1 (MF-10), the corresponding MWCNT-Fe_3O_4@Ag/epoxy nanocomposites presented the optimal electrical conductivity and EMI SE. Furthermore, the MF-10/epoxy nanocomposites with 15 wt% MF-10 presented the excellent EMI SE of 35 dB and high electrical conductivity of 0.280 S/cm, satisfactory λ of 0.46 W/mK, outstanding Young's modulus of 4.60 GPa & hardness value of 0.26 GPa and excellent thermal stability (T_{HRI} of 183.4 °C). The excellent comprehensive properties make the ob-

Table 6
Characteristic thermal data of MF-10/epoxy nanocomposites at air condition.

Samples	Weight loss temperature(°C)			$T_{\text{Heat-resistance index}}$[a] (°C)	Residue (%)
	T_5	T_{30}	T_{50}		
1 wt% MF-10/epoxy	265.8	385.2	443.2	167.7	0.14
5 wt% MF-10/epoxy	283.3	384.4	453.6	168.5	0.32
10 wt% MF-10/epoxy	338.1	383.1	464.8	178.9	0.72
15 wt% MF-10/epoxy	352.3	388.9	476.7	183.4	1.22

[a] The sample's heat-resistance index is calculated by Equation (1).

Effects of mass fraction of MF-10 on the hardness and Young's modulus of the MF-10/epoxy nanocomposites are presented in Fig. 7. The decreased indentation depth (Fig. 7(a)) of the MF-10/epoxy nanocomposites revealed their enhanced ability to resist the indentation with increasing the addition of MF-10 [61]. In Fig. 7(b), compared to that of MF-10/epoxy nanocomposites with 1 wt% MF-10, the Young's modulus of the MF-10/epoxy nanocomposites with 15 wt% MF-10 was increased from 4.28 to 4.60 GPa, and the corresponding hardness was also enhanced from 0.23 to 0.28 GPa. There was a strong interaction between the MF-10 and the epoxy due to the existence of reactive groups on the MF-10. Therefore, the hardness and Young's modulus of the MF-10/epoxy nanocomposites were improved with the addition of MF-10. As a result, the addition of MF-10 was in favor of increasing the Young's modulus and hardness of the MF-10/epoxy nanocomposites.

Fig. 8 depicts the TGA curves of MF-10/epoxy nanocomposites at air condition, and the corresponding characteristic thermal data were shown in Table 6. The thermal decomposition of the all above epoxy nanocomposites took place in two stages. Epoxy resins was broken down in the first stage from 300 to 400 °C, and benzene rings in the epoxy backbone were degraded in the second stage from 450 to 600 °C. All the T_5, T_{30} and T_{50} values were increased with increasing the addition of MF-10, and the T_{HRI} [62] value of the MF-10/epoxy nanocomposites with 15 wt% MF-10 was obviously increased from 167.7 °C for MF-10/epoxy nanocomposites with 1 wt% MF-10 to 183.4 °C. It confirmed that the thermal stabilities of the MF-10/epoxy nanocomposites were gradually increased with increasing the addition of MF-10.

$$T_{Heat\text{-}resistance\ index} = 0.49*[T_5 + 0.6*(T_{30} - T_5)] \tag{1}$$

tained MWCNT-Fe_3O_4@Ag/epoxy nanocomposites suitable for broad applications such as medical equipment, industrial electronic equipment, wireless base stations and aviation equipment.

References

[1] F. Wu, M. Sun, W. Jiang, K. Zhang, A. Xie, Y. Wang, M. Wang, A self-assembly method for the fabrication of a three-dimensional (3D) polypyrrole (PPy)/poly(3,4-ethylenedioxythiophene) (PEDOT) hybrid composite with excellent absorption performance against electromagnetic pollution, J. Mater. Chem. C 4 (1) (2015) 82–88.

[2] C. Liu, Y. Xu, L. Wu, Z. Jiang, B. Shen, Z. Wang, Fabrication of core-multishell MWCNT/Fe₃O₄/PANI/Au hybrid nanotubes with high-performance electromagnetic absorption, J. Mater. Chem. 3 (19) (2015) 10566–10572.

[3] Z. Chen, C. Xu, C. Ma, W. Ren, H.M. Cheng, Lightweight and flexible graphene foam composites for high-performance electromagnetic interference shielding, Adv. Mater. 25 (9) (2013) 1296–1300.

[4] N. Li, Y. Huang, F. Du, X. He, X. Lin, H. Gao, Y. Ma, F. Li, Y. Chen, P.C. Eklund, Electromagnetic interference (EMI) shielding of single-walled carbon nanotube epoxy composites, Nano Lett. 6 (6) (2006) 1141–1145.

[5] L.L. Wang, B.K. Tay, K.Y. See, Z. Sun, L.K. Tan, D. Lua, Electromagnetic interference shielding effectiveness of carbon-based materials prepared by screen

printing, Carbon 47 (8) (2009) 1905–1910.

[6] N. Yousefi, X. Sun, X. Lin, X. Shen, J. Jia, B. Zhang, B. Tang, M. Chan, J.K. Kim, Highly aligned graphene/polymer nanocomposites with excellent dielectric properties for high-performance electromagnetic interference shielding, Adv. Mater. 26 (31) (2015) 5480–5487.

[7] B. Shen, W. Zhai, W. Zheng, Ultrathin flexible graphene film: an excellent thermal conducting material with efficient EMI shielding, Adv. Funct. Mater. 24 (28) (2014) 4542–4548.

[8] F. Ye, Q. Song, Z. Zhang, W. Li, S. Zhang, X. Yin, Y. Zhou, H. Tao, Y. Liu, L. Cheng, Direct growth of edge-rich graphene with tunable dielectric properties in porous Si₃N₄ ceramic for broadband high-performance microwave absorption, Adv. Funct. Mater. 20 (2018) 1707205.

[9] Y. Huang, N. Li, Y. Ma, F. Du, F. Li, X. He, X. Lin, H. Gao, Y. Chen, The influence of single-walled carbon nanotube structure on the electromagnetic interference shielding efficiency of its epoxy composites, Carbon 45 (8) (2007) 1614–1621.

[10] Y. Liu, D. Song, C. Wu, J. Leng, EMI shielding performance of nanocomposites with MWCNTs, nanosized Fe₃O₄ and Fe, Compos. B Eng. 63 (7) (2014) 34–40.

[11] J. Li, Y. Xie, W. Lu, T.W. Chou, Flexible electromagnetic wave absorbing composite based on 3D rGO-CNT-Fe₃O₄ ternary films, Carbon 129 (2018) 76–84.

[12] B.P. Singh, D.K. Saket, A.P. Singh, S. Pati, T.K. Gupta, V.N. Singh, S.R. Dhakate, S.K. Dhawan, R.K. Kotnala, R.B. Mathur, Microwave shielding properties of Co/Ni attached to single walled carbon nanotubes, J. Mater. Chem. 3 (25) (2015) 13203–13209.

[13] Y. Yin, X. Liu, X. Wei, R. Yu, J. Shui, Porous CNTs/Co composite derived from zeolitic imidazolate framework: a Lightweight, ultrathin and highly efficient electromagnetic wave absorber, ACS Appl. Mater. Interfaces 8 (50) (2016) 34686–34698.

[14] Y. Chen, Y. Wang, H.B. Zhang, X. Li, C.X. Gui, Z.Z. Yu, Enhanced electromagnetic interference shielding efficiency of polystyrene/graphene composites with magnetic Fe₃O₄ nanoparticles, Carbon 82 (2015) 67–76.

[15] P.R. Agarwal, R. Kumar, S. Kumari, S.R. Dhakate, Three-dimensional and highly ordered porous carbon-MnO₂ composite foam for excellent electromagnetic interference shielding efficiency, RSC Adv. 6 (103) (2016) 100713–100722.

[16] J.M. Perez, Iron oxide nanoparticles: hidden talent, Nat. Nanotechnol. 2 (9) (2007) 535.

[17] X. Jian, B. Wu, Y. Wei, S.X. Dou, X. Wang, W. He, N. Mahmood, Facile synthesis of Fe₃O₄/GCs composites and their enhanced microwave absorption properties, ACS Appl. Mater. Interfaces 8 (9) (2016) 6101–6109.

[18] N. Li, G.W. Huang, Y.Q. Li, H.M. Xiao, Q.P. Feng, N. Hu, S.Y. Fu, Enhanced microwave absorption performance of coated carbon nanotubes by optimizing the Fe₃O₄ nanocoating structure, ACS Appl. Mater. Interfaces 9 (3) (2017) 2973–2983.

[19] A. Chaudhary, R. Kumar, S. Teotia, S. Dhawan, S.R. Dhakate, S. Kumari, Integration of MCMBs/MWCNTs with Fe₃O₄ in a flexible and light weight composite paper for promising EMI shielding applications, J. Mater. Chem. C 5 (2) (2017) 322–332.

[20] J. Ma, K. Wang, M. Zhan, Growth mechanism and electrical and magnetic properties of Ag-Fe₃O₄ core-shell nanowires, ACS Appl. Mater. Interfaces 7 (29) (2015) 16027–16039.

[21] B. Zhao, Z. Nan, Enhancement of electric conductivity by incorporation of Ag into core/shell structure of Fe₃O₄/Ag/PPy NPs, Mater. Sci. Eng. C 32 (4) (2012) 804–810.

[22] Y. Sun, Y. Tian, M. He, Q. Zhao, C. Chen, C. Hu, Y. Liu, Controlled synthesis of Fe₃O₄/Ag Core-Shell composite nanoparticles with high electrical conductivity, J. Electron. Mater. 41 (3) (2012) 519–523.

[23] J.X. Zhang, Y.X. Liang, X. Wang, H.J. Zhou, S.Y. Li, J. Zhang, Y. Feng, N. Lu, Q. Wang, Z. Guo, Strengthened epoxy resin with hyperbranched polyamine-ester anchored graphene oxide via novel phase transfer approach, Adv. Compos. Hybrid. Mater. 1 (2017) 1–10.

[24] X. Yang, Y. Guo, X. Luo, N. Zheng, T. Ma, J. Tan, C. Li, Q. Zhang, J. Gu, Self-healing, recoverable epoxy elastomers and their composites with desirable thermal conductivities by incorporating BN fillers via in-situ polymerization, Compos. Sci. Technol. 164 (2018) 59–64.

[25] J. Chen, X. Huang, Y. Zhu, P. Jiang, Cellulose nanofiber supported 3D interconnected BN nanosheets for epoxy nanocomposites with ultrahigh thermal management capability, Adv. Funct. Mater. 27 (5) (2017) 1604754.

[26] C. Liang, P. Song, H. Gu, C. Ma, H. Zhang, X. Xu, Q. Zhang, J. Gu, Nano-polydopamine coupled fluorescent nanozinc oxide reinforced epoxy nanocomposites, Compos. Part A-Appl. S. 102 (2017) 126–136.

[27] D. Sun, J. An, G. Wu, J. Yang, Double-layered reactive microcapsules with excellent thermal and non-polar solvent resistance for self-healing coatings, J. Mater. Chem. 3 (8) (2015) 4435–4444.

[28] Y. Yan, S.C. Warren, P. Fuller, B.A. Grzybowski, Chemoelectronic circuits based on metal nanoparticles, Nat. Nanotechnol. 11 (7) (2016) 603–608.

[29] Q. Zhuang, D.A. Walker, K.P. Browne, B. Kowalczyk, G. Beniah, B.A. Grzybowski, Temperature driven assembly of like-charged nanoparticles at non-planar liquid-liquid or gel-air interfaces, Nanoscale 6 (9) (2014) 4475–4479.

[30] J. Gu, L. Wang, C. Liang, Q. Zhuang, J. Kong, Controlled shell on nanoparticles as a tool to regulate the properties of immobilized molecules, J. Alloy. Comp. 745 (2018) 430–435.

[31] K. Yang, H. Peng, Y. Wen, N. Li, Re-examination of characteristic FTIR spectrum of secondary layer in bilayer oleic acid-coated Fe₃O₄ nanoparticles, Appl. Surf. Sci. 256 (10) (2010) 3093–3097.

[32] D.L. Zhao, X.X. Wang, X.W. Zeng, Q.S. Xia, J.T. Tang, Preparation and inductive heating property of Fe₃O₄-chitosan composite nanoparticles in an AC magnetic field for localized hyperthermia, J. Alloy. Comp. 477 (1) (2009) 739–743.

[33] P. Jiang, Z.F. Liu, S.M. Cai, Growing monodispersed PbS nanoparticles on self-assembled monolayers of 11-mercaptoundecanoic acid on Au (111) substrate, Langmuir 18 (11) (2002) 4495–4499.

[34] S.K. Park, K. Choi, S.H. Lee, I.K. Oh, S. Park, H.S. Park, CNT branching of three-dimensional steam-activated graphene hybrid frameworks for excellent rate and cyclic capabilities to store lithium ions, Carbon 116 (2017) 500–509.

[35] B.M. Amoli, S. Gumfekar, A. Hu, Y.N. Zhou, B. Zhao, Thiocarboxylate functionalization of silver nanoparticles: effect of chain length on the electrical conductivity of nanoparticles and their polymer composites, J. Mater. Chem. 22 (37) (2012) 20048–20056.

[36] J. Jiang, H. Gu, H. Shao, E. Devlin, G.C. Papaefthymiou, J.Y. Ying, Bifunctional Fe₃O₄-Ag heterodimer nanoparticles for two-photon fluorescence imaging and magnetic manipulation, Adv. Mater. 20 (23) (2008) 4403–4407.

[37] S.Y. Mak, D.H. Chen, Binding and sulfonation of poly (acrylic acid) on Iron oxide nanoparticles: a novel, magnetic, strong acid cation nano-adsorbent, Macromol. Rapid Commun. 26 (19) (2005) 1567–1571.

[38] C.H. Liu, Z.D. Zhou, X. Yu, B.Q. Lv, J.F. Mao, D. Xiao, Preparation and characterization of Fe₃O₄/Ag composite magnetic nanoparticles, Inorg. Mater. 44 (3) (2008) 291–295.

[39] B. Yu, P.X. Hou, F. Li, B. Liu, C. Liu, H.M. Cheng, Selective removal of metallic single-walled carbon nanotubes by combined in situ and post-synthesis oxidation, Carbon 48 (10) (2010) 2941–2947.

[40] H. Veisi, F.H. Eshbala, S. Hemmati, M. Baghayeri, Selective hydrogen peroxide oxidation of sulfides to sulfones with carboxylated multi-walled carbon nano tubes (MWCNTs-COOH) as heterogeneous and recyclable nanocatalysts under organic solvent-free conditions, RSC Adv. 5 (14) (2015) 10152–10158.

[41] F. Giacalone, V. Campisciano, C. Calabrese, V. La Parola, Z. Syrgiannis, M. Prato, M. Gruttadauria, Single-walled carbon nanotube-polyamidoamine dendrimer hybrids for heterogeneous catalysis, ACS Nano 10 (4) (2016) 4627–4636.

[42] A. Jędrzak, T. Rębiś, Ł. Klapiszewski, J. Zdarta, G. Milczarek, T. Jesionowski, Carbon paste electrode based on functional GOx/silica-lignin system to prepare an amperometric glucose biosensor, Sens. Actuators, B 256 (2018) 176–185.

[43] J. Wang, C. Zhang, Z. Du, H. Li, W. Zou, Functionalization of MWCNTs with silver nanoparticles decorated polypyrrole and their application in antistatic and thermal conductive epoxy matrix nanocomposite, RSC Adv. 6 (38) (2016) 31782–31789.

[44] R. Sedghi, Z. Pezeshkian, Fabrication of non-enzymatic glucose sensor based on nanocomposite of MWCNTs-COOH-Poly (2-aminothiophenol)-Au NPs, Sens. Actuators, B 219 (2015) 119–124.

[45] X. Chen, X. Chen, M. Lin, W. Zhong, X. Chen, Z. Chen, Functionalized multi-walled carbon nanotubes prepared by in situ polycondensation of polyurethane, Macromol. Chem. Phys. 208 (9) (2007) 964–972.

[46] M. Yang, L. Hu, X. Tang, H. Zhang, H. Zhu, T. Fan, D. Zhang, Longitudinal splitting versus sequential unzipping of thick-walled carbon nanotubes: towards controllable synthesis of high-quality graphitic nanoribbons, Carbon 110 (2016) 480–489.

[47] S.Y. Yang, C.C.M. Ma, C.C. Teng, Y.W. Huang, S.H. Liao, Y.L. Huang, H.W. Tien, T.M. Lee, K.C. Chiou, Effect of functionalized carbon nanotubes on the thermal conductivity of epoxy composites, Carbon 48 (3) (2010) 592–603.

[48] T. Wang, Z. Liu, M. Lu, B. Wen, Q. Ouyang, Y. Chen, C. Zhu, P. Gao, C. Li, M. Cao, Graphene-Fe₃O₄ nanohybrids: synthesis and excellent electromagnetic absorption properties, J. Appl. Phys. 113 (2) (2013) 024314.

[49] A.P. Singh, B.K. Gupta, M. Mishra, A. Chandra, R. Mathur, S. Dhawan, Multi-walled carbon nanotube/cement composites with exceptional electromagnetic interference shielding properties, Carbon 56 (2013) 86–96.

[50] P. Verma, P. Saini, R.S. Malik, V. Choudhary, Excellent electromagnetic interference shielding and mechanical properties of high loading carbon-nanotubes/polymer composites designed using melt recirculation equipped twin-screw extruder, Carbon 89 (2015) 308–317.

[51] D. Chung, Electromagnetic interference shielding effectiveness of carbon materials, Carbon 39 (2) (2001) 279–285.

[52] P.K.S. Mural, S.P. Pawar, S. Jayanthi, G. Madras, A.K. Sood, S. Bose, Engineering nanostructures by decorating magnetic nanoparticles onto Graphene Oxide Sheets to shield electromagnetic radiations, ACS Appl. Mater. Interfaces 7 (30) (2015) 16266–16278.

[53] M. Arjmand, A.A. Moud, Y. Li, U. Sundararaj, Outstanding electromagnetic interference shielding of silver nanowires: comparison with carbon nanotubes, RSC Adv. 5 (70) (2015) 56590–56598.

[54] X. Jiang, D.X. Yan, Y. Bao, H. Pang, X. Ji, Z.M. Li, Facile, green and affordable strategy for structuring natural graphite/polymer composite with efficient electromagnetic interference shielding, RSC Adv. 5 (29) (2015) 22587–22592.

[55] J. Liang, Y. Wang, Y. Huang, Y. Ma, Z. Liu, J. Cai, C. Zhang, H. Gao, Y. Chen, Electromagnetic interference shielding of graphene/epoxy composites, Carbon 47 (3) (2009) 922–925.

[56] B. Shen, W. Zhai, M. Tao, J. Ling, W. Zheng, Lightweight, multifunctional polyetherimide/graphene@Fe₃O₄ composite foams for shielding of electromagnetic pollution, ACS Appl. Mater. Interfaces 5 (21) (2013) 11383–11391.

[57] Z. Liu, G. Bai, Y. Huang, Y. Ma, F. Du, F. Li, T. Guo, Y. Chen, Reflection and absorption contributions to the electromagnetic interference shielding of single-walled carbon nanotube/polyurethane composites, Carbon 45 (4) (2007) 821–827.

[58] M.S. Cao, J. Yang, W.L. Song, D.Q. Zhang, B. Wen, H.B. Jin, Z.L. Hou, J. Yuan, Ferroferric oxide/multiwalled carbon nanotube vs polyaniline/ferroferric oxide/multiwalled carbon nanotube multiheterostructures for highly effective microwave absorption, ACS Appl. Mater. Interfaces 4 (12) (2012) 6949—6956.

[59] J. Gu, Z. Lv, Y. Wu, Y. Guo, L. Tian, H. Qiu, W. Li, Q. Zhang, Dielectric thermally conductive boron nitride/polyimide composites with outstanding thermal stabilities via in-situ polymerization-electrospinning-hot press method, Compos. Part A-Appl. S. 94 (2017) 209—216.

[60] X. Yang, L. Tang, Y. Guo, C. Liang, Q. Zhang, K. Kou, J. Gu, Improvement of thermal conductivities for PPS dielectric nanocomposites via incorporating NH$_2$-POSS functionalized nBN fillers, Compos. Part A-Appl. S. 101 (2017) 237—242.

[61] S.L. Gao, E. Mäder, S.F. Zhandarov, Carbon fibers and composites with epoxy resins: topography, fractography and interphases, Carbon 42 (3) (2004) 515—529.

[62] Y. Tang, W. Dong, L. Tang, Y. Zhang, J. Kong, J. Gu, Fabrication and investigations on the polydopamine/KH-560 functionalized PBO fibers/cyanate ester wave-transparent composites, Compos. Commun. 8 (2018) 36—41.